SIMULATION OF POWDER METAL FABRICATION WITH HIGH PRESSURE GAS ATOMIZATION

David W. Kuntz
Thermophysics Department

Jeffrey L. Payne
Aerosciences and Fluid Dynamics Department

Sandia National Laboratories
Albuquerque, New Mexico 87185

ABSTRACT

A computational/analytical technique has been developed which models the physics of high pressure gas atomization. The technique uses an uncoupled approach, such that the gas flowfield is initially calculated with a commercially-available Navier-Stokes code. The liquid metal droplet breakup, dynamics, and thermodynamics, are then calculated using the pre-computed flowfield by a separate computer program written by the authors. The atomization code models the primary breakup of the liquid metal stream, tracks the droplets resulting from primary breakup through the flowfield until they undergo secondary breakup, and then tracks the subdroplets until they breakup, solidify, or leave the flowfield region of interest. The statistical properties of the metal powder produced are then computed from the characteristics of these droplets. Comparisons between experimental measurements and computations indicate that the Navier-Stokes code is predicting the gas flowfield well, and that the atomization code is properly modeling the physics of the droplet dynamics and breakup.

NOMENCLATURE

a,b	Exponents used in particle mean size calculations [-]
d, D	Diameter [m]
GLR	Gas to liquid mass flow rate ratio [-]
L	Length [m]
$\dot{m}$	Mass flow rate [kg/s]
MMD	Mass median diameter [m]
N	Number of particles [-]
Oh	Ohnesorge number [-]
R	Radial coordinate measured from the nozzle centerline [m]
Re	Reynolds number [-]
SMD	Sauter median diameter [m]
t	Time [s]
t*	Characteristic droplet breakup time [s]

DISCLAIMER

t_C*	Corrected characteristic droplet breakup time [s]
U_{rel}	Relative velocity between the gas and the liquid [m/s]
V	Velocity component in the radial direction [m/s]
We	Weber number [-]
X	Axial coordinate measured from the gas nozzle exit [m]
ε	Sheet breakup parameter [see Equation 7]
μ	Dynamic viscosity [N-s/m^2]
ρ	Density [kg/m^3]
σ	Surface tension [N/m]
τ	Film or sheet thickness [m]

Subscripts

b	Breakup property
c	Cross-stream value
d	Droplet property
e	Edge condition
f	Film property
g	Gas property
i	Particle size range index
L	Liquid property
max	Maximum value
s	Sheet property
0	Undeformed value

INTRODUCTION

The fabrication of metal powders with high pressure gas atomization is a widely used technique for producing powders with a broad range of alloy compositions. The phenomena which occur within this type of atomization are very complicated and involve high speed compressible fluid mechanics, primary and secondary droplet breakup, and droplet dynamics and thermodynamics. A computational/analytical technique has been developed which models the atomization process. The technique uses an uncoupled approach in which the gas flowfield is initially calculated with the INCA[1] code, a commercially-available program which solves the full Navier-Stokes equations. The properties of the liquid metal as it is atomized by the high velocity gas stream are then calculated with a separate program which uses the INCA solution as an input and tracks the liquid metal through the gas flowfield. Correlations are used within the atomization code along with the basic conservation equations to calculate the final properties of the liquid metal droplets, and thus the properties of the metal powder produced by the atomization process.

ATOMIZER GEOMETRY

The atomizer geometry, illustrated in Figure 1, is essentially an axisymmetric representation of the nozzle used at both the National Institute of Standards and Technology (NIST) and at Ames Laboratory[2]. The nozzle consists of a liquid metal delivery tube surrounded by an annular gas nozzle. The NIST/Ames configuration consists of 18 separate gas nozzles which have been replaced in this study by the single annular nozzle of equal area. Details of the flowfield produced by this type of nozzle will be illustrated later in this report.

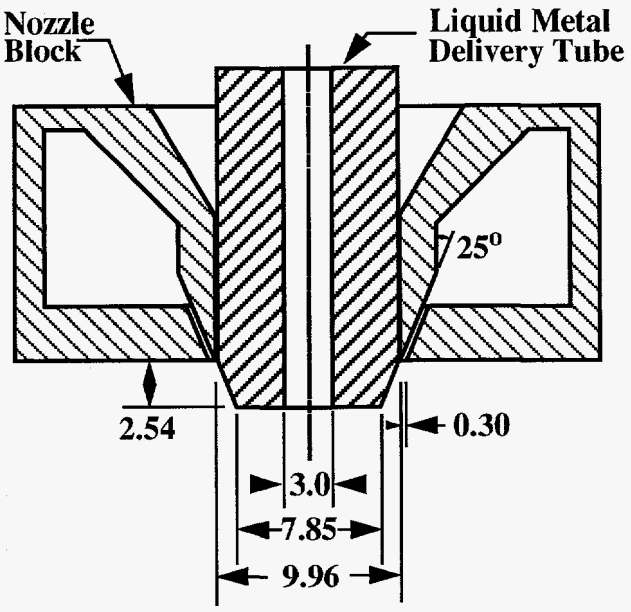

Figure 1: Nozzle Geometry (all dimensions in mm).

GAS FLOWFIELD SOLUTION TECHNIQUE

The flowfields within liquid metal atomizers are extremely complex, and often include regions of supersonic flow, shock waves, free shear layers, and separated flow. As a result, it is necessary to solve for the gas flowfield using the Navier-Stokes equations. Several computer programs are commercially available which can solve these flowfields. The code used in this study was the INCA[1] program. This program uses an implicit finite-volume method to solve the conservative form of the two-dimensional, two-dimensional axisymmetric, or three-dimensional Navier-Stokes equations. The code can treat the gas as an ideal gas, a real gas, or a real gas with chemical reactions. The flow can be either laminar or turbulent, with several turbulence models available.

The finite-volume formulation of the INCA code requires that the equations be solved on a grid within the flowfield domain. Efficient computation requires that the grid be relatively fine in regions with large gradients of flowfield properties, and relatively coarse in regions with small changes in flowfield properties. Since exact details of the flowfield are not known a priori, the computational grid must be refined periodically during the flowfield computations. This is done by partially solving the flowfield using the INCA program, and then refining the grid based on the current INCA solution using the SAGE program described in Reference 3.

GAS FLOWFIELD SOLUTION

The flowfield solution for the geometry shown in Figure 1 was computed using atomizer conditions obtained from NIST[4] and listed in Table 1. These conditions were used so that a direct comparison between measurements of the powder produced by the NIST atomizer and the results of the current analysis could be made. The Reynolds number at the nozzle exit based on the NIST operating conditions is relatively high such that the gas flow is expected to be turbulent within the flowfield which develops downstream of the nozzle exit. The INCA solution for the axisymmetric gas flowfield was obtained using the Baldwin-Barth one-equation turbulence model[5]. Although the k-ε turbulence model[6] could be expected to give more accurate results in flowfields of this type, significant difficulties in obtaining a converged solution were encountered using this model in the INCA code.

Table 1: NIST Atomizer Conditions

Gas	Argon
Plenum Pressure	5.50×10^6 Pa (798 psia)
Plenum Temperature	264 K (475 °R)
Atomizing Chamber Pressure	1.034×10^5 Pa (15 psia)
Gas Mass Flow Rate	0.140 kg/s (0.309 lbm/s)
Metal	Inconel 625
Metal Temperature	1,951 K (3,512 °R)
Metal Mass Flow Rate	0.0375 kg/s (0.0827 lbm/s)
Gas to Metal Mass Flow Rate Ratio	3.74

The gas flowfield was computed using a grid totaling 52,893 grid points. The computational domain extended axially from within the nozzle plenum chamber to a location 0.30 m downstream of the exit of the gas nozzle, and radially from the nozzle centerline to a location 0.10 m from the nozzle centerline.

The Mach number distribution computed by the INCA code is shown in Figure 2. The flow reaches Mach 1 at the nozzle exit as the flow chokes, and then accelerates to a maximum Mach number of 6.0 as the flow expands into the atomization chamber. The flow separates at the corner of the liquid metal delivery tube and forms an annular free jet until the flow converges on the centerline approximately 0.025 m downstream of the gas nozzle exit to form a single annular jet. The flow within the separated region, illustrated in Figure 3, has a relatively low velocity as it flows (in Figure 3) from right to left along the centerline, up the face of the liquid metal delivery tube, and along the inside edge of the annular jet. The existence of this separated region has a large effect on the atomization process and has been visualized in Schlieren photographs of this nozzle configuration[2,7] as well as other similar nozzle configurations[8,9].

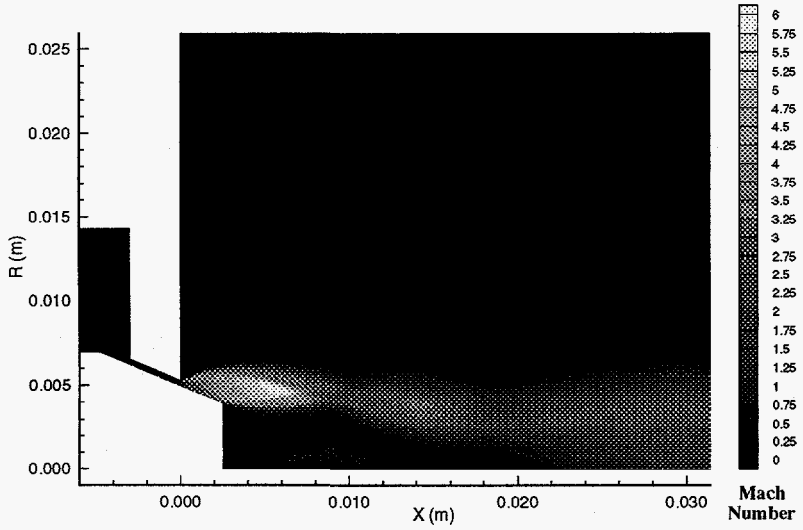

Figure 2: Computed Mach Number Contours.

LIQUID METAL DROPLET SOLUTION TECHNIQUE

The code which calculates the characteristics of the liquid metal as it undergoes atomization uses the INCA flowfield solution as input. Thus the solution is considered uncoupled, in that the effects of the liquid metal on the flowfield are not accounted for in the solution technique. Although an exchange of momentum and energy between the gas and the droplets does occur and thus the gas flowfield is affected

by liquid, reasonably accurate solutions can be obtained from an uncoupled solution at a fraction of the computational cost of a fully coupled solution. This is supported by Schlieren photographs included in Reference 8 which compare a gas-only flowfield with a flowfield atomizing water under the same conditions. The photographs show nearly identical shock structures and shear layer shapes, indicating that the water droplets have very little effect on the gas flowfield.

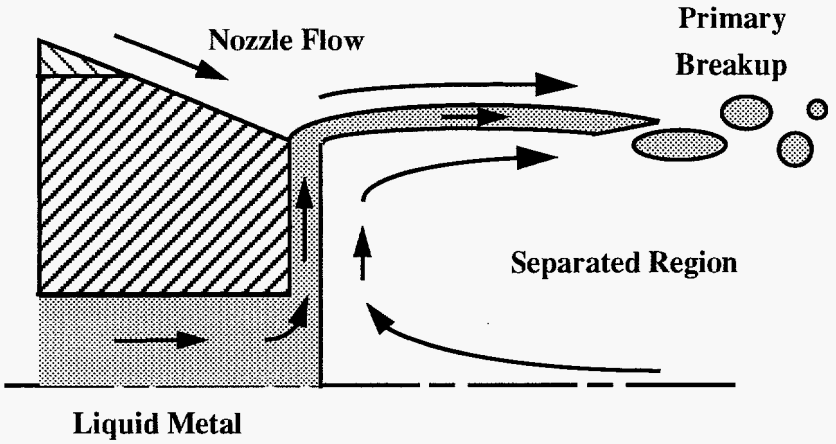

Figure 3: Primary Breakup Model

The solution procedure within the atomization code involves following the liquid metal step by step as it proceeds through the atomization process. The initial step is the calculation of the liquid metal film which forms on the tip of the liquid metal delivery tube. The presence of this film is the result of the separated flow which is directed radially outward from the centerline of the nozzle. This separated flow causes the liquid to flow radially outward from the exit of the tube to the tube perimeter where the atomization process begins to take place. The existence of this film has been confirmed experimentally in both this nozzle configuration[2] and other similar nozzle configurations[8,10].

The second step in the computation of the atomization process is modeling the primary breakup, which occurs when the liquid film interacts with the annular high velocity gas stream. High speed videos made of the atomization process at the NIST facilities, as well as high speed films made by Anderson as described in Reference 2, indicate that the film turns due to the influence of the gas stream and becomes a sheet of liquid initiating from the edge of the tube face and extending parallel to the gas flow. This sheet is highly unsteady and can vary from a length of essentially zero to a length extending a significant distance downstream into the flowfield. This process ends with primary breakup as the sheet fragments into relatively large droplets.

The third step of the solution procedure involves calculating the trajectories and temperature histories of the large droplets produced by the primary breakup process as they move through the flowfield. These droplets are followed until they undergo secondary breakup, cool to the solidification temperature, or exit the computational domain. The characteristics of the droplets produced by secondary breakup are computed as these droplets move through the flowfield in a manner identical to those of the droplets produced by primary breakup. These droplets are followed until they also undergo breakup, cool to the solidification temperature, or exit the computational domain. These procedures are continued until the characteristics of all droplets have been computed. At this point, the droplets are numerically sieved and final statistics for the resultant powder are computed.

Film Model

The characteristics of the liquid metal film flowing radially on the face of the delivery tube (shown flowing vertically upward on Figure 3) are calculated using a force balance technique. It is assumed that the film is not accelerating, and thus the shear force imposed on the film by the gas flowing radially outward in the separated region must be balanced by the shear force between the flowing liquid metal film and the end of the delivery tube. The additional assumption that the velocity distribution within the film is

linear (Couette flow) results in the following equations for the thickness of the film and the velocity of the film at the surface where it contacts the separated gas flowfield.

$$\tau_f(R) = \left[\frac{\mu_L}{\mu_g(R)} \frac{\dot{m}_L}{\pi \rho_L R \frac{dV_g}{dX}(R)} \right]^{1/2} \quad (1)$$

$$V_{L,e}(R) = \frac{\dot{m}_L}{\pi \rho_L R} \left[\frac{\mu_g(R)}{\mu_L} \frac{\pi \rho_L R \frac{dV_g}{dX}(R)}{\dot{m}_L} \right]^{1/2} \quad (2)$$

Since the velocity distribution within the film is assumed to be linear, the mean film velocity is equal to one-half of the film edge velocity, $V_{L,e}$. The gas properties in the equations above are obtained from the INCA flowfield solution, and the liquid properties are those of the liquid metal at its initial temperature. The film velocity and thickness are evaluated at a radial location near the edge of the delivery tube and are used as inputs for the primary breakup model, described below.

Primary Breakup Model

The primary breakup model consists of two sub-models, one modeling the formation and trajectory of the liquid metal sheet, and one modeling the breakup of the sheet into droplets.

Sheet Formation

The sheet is assumed to start at the edge of the delivery tube with an initial thickness equal to the film thickness, an initial velocity in the radial direction equal to the mean film velocity, and an initial temperature equal to the liquid metal initial temperature. The trajectory of the sheet is calculated by summing the forces imposed upon the sheet by the surrounding flowfield, and integrating the equations of motion for the sheet in time. Two types of forces are imposed on the sheet: shear forces and pressure forces. The shear forces result from the gas flowing parallel to the sheet surface. The magnitude of these forces are calculated using laminar flat plate boundary layer theory obtained from White[11]. The pressure forces on the sheet act on the inner and outer surfaces of the sheet perpendicular to the sheet surface. The pressure on the windward side of the sheet, the side of the sheet with the gas impinging on the sheet surface, is calculated using two-dimensional, oblique shock wave theory[12]. The pressure on the leeward side of the sheet, the side of the sheet with the gas moving away from the sheet surface, is calculated using two-dimensional, Prandtl-Meyer expansion theory[12]. A difference in pressure forces across the sheet occurs only when there is a misalignment between the gas flowfield and the sheet, and thus the pressure forces cause the sheet to align with the flow while the shear forces cause the sheet to accelerate downstream within the gas flowfield.

The temperature of the sheet is calculated by integrating the energy equation in time. The heating rate is obtained from laminar flat plate boundary layer relations obtained from White[11].

The mean length of the sheet is calculated using a correlation developed by Arai and Hashimoto[13] and reported by Eroglu, Chigier, and Farago[14]. This empirical correlation was developed from experimental data obtained with a thin water sheet in a cocurrent high-speed air stream and can be written as:

$$L_s = 1.23 \tau_s^{0.5} We_s^{-0.5} Re_s^{0.6} \quad (3)$$

$$We_s = \left(\tau_s \rho_g U_{rel}^2 \right) / (2\sigma_L) \quad (4)$$

$$Re_s = (\tau_s U_L \rho_L) / \mu_L \quad (5)$$

The extensive amount of unsteadiness in the sheet length seen in the high-speed videos taken at the NIST facility indicates that to terminate the sheet at its mean length would be an over-simplification. In order to model the unsteadiness of the sheet, sheet trajectory calculations are carried out to a length equal to twice the mean length calculated by the relation shown above. Primary breakup is then modeled as occurring over this entire sheet length uniformly by dividing the sheet into equal length segments and then releasing equal amounts of liquid metal from each of these segments.

Sheet Breakup

The primary breakup of each of the sheet segments is modeled in order to produce the relatively large droplets which are initially released into the flowfield. The droplet size distribution after primary breakup is assumed to fit Simmons'[15] universal root-normal distribution based on the work of Wu, Ruff, and Faeth[16]. Wu, Ruff, and Faeth studied the primary breakup of large-diameter liquid jets in still air. Their results indicated that the size distribution of the droplets after primary breakup, but prior to any secondary breakup, fits Simmons' universal root-normal distribution with a ratio of mass median diameter to Sauter mean diameter (MMD/SMD) equal to 1.2. This distribution is characterized by a straight line fit when $\sqrt{d/MMD}$ is plotted as a function of cumulative volume on a normal probability scale. The ratio MMD/SMD specifies the slope of the line, and assuming this distribution, only the Sauter mean diameter needs to be determined to completely specify the droplet size distribution.

The Sauter mean diameter of the droplet distribution resulting from the sheet breakup is determined using a semi-empirical correlation developed by Knoll and Sojka[17]. Knoll and Sojka studied the disintegration of a flat liquid sheet in coflowing air streams and determined:

$$SMD = \frac{12\sigma_L}{\left[\left(\rho_L U^2_{rel}\right)/(1+1/(\varepsilon GLR))\right] + 4\frac{\sigma_L}{\tau_s}} \tag{6}$$

where

$$\varepsilon = \frac{1.62}{U_g^{1.30} GLR^{0.63} \mu_L^{0.30}} \tag{7}$$

The equation for SMD (Equation 6) is dimensionally consistent, but the equation for ε (Equation 7) is not, and the units referred to in the nomenclature must be used in this relation.

With the SMD calculated, each of the sheet segments is broken up consistent with its properties (i.e. thickness, viscosity, surface tension) and the local flow conditions. The breakup is performed by distributing the sheet segment mass into bins, each of which represents droplets within a fixed size range. The amount of mass in each bin, and thus the number of droplets represented by each bin, is determined using the root-normal distribution. Each bin is then treated as a single computational droplet (representing multiple real droplets) for the remaining computations, and is released into the flowfield at the location and with the velocity and temperature of the sheet segment from which it originated.

Droplet Dynamics and Thermodynamics Models

Droplet Dynamics

The dynamics of the computational droplets are determined by integrating the equations of motion in time as the droplets proceed through the pre-calculated flowfield. The equations model a sphere in a viscous fluid and can be found in detail in Reference 18. The equations include terms for the viscous drag, the pressure gradient force, the apparent mass force, the Basset history force, and the gravitational force. Each of these terms are used in the integration, with the exception of the Basset history force which is small and difficult to implement accurately.

The drag coefficient used to determine the viscous drag force is computed by linearly interpolating between the drag coefficients of a sphere and a disk, depending upon the droplet's distortion. The drag

coefficient for a sphere is determined using the relations of Henderson[19]. These relations are functions of droplet Reynolds number (based on relative velocity), Mach number (based on relative velocity), droplet temperature, flowfield temperature, and the flowfield specific heat ratio. Henderson's relations were chosen because of their excellent agreement with the experimental data of Bailey and Hiatt[20]. The drag coefficient of a disk was obtained as a function of Reynolds number from Figure 3-26 of Reference 21, and corrected for Mach number effects using Figure 18-38 of the same reference.

Droplet Thermodynamics

The temperature of the droplet has a significant effect on its properties and thus on its breakup characteristics. In order to account for temperature variations in droplets with time, a form of the energy equation is integrated in time along with the equations of motion. As a result of the relatively high thermal conductivity of liquid metals, the droplets are assumed to be at a uniform temperature. The energy equation includes terms for both convection and radiation. The convection heating/cooling is calculated by first calculating the heat transfer rate at the droplet stagnation point using compressible sphere heating relations found in Reference 11. The ratio of average sphere heating to stagnation point heating is then calculated using relations presented in Reference 22.

The radiative component of droplet heating/cooling is computed assuming that the atomizing chamber is at a single temperature and that the droplet exchanges heat with the chamber walls and not with other droplets. This reduces the radiative heating/cooling to a relatively simple computation which is only a function of the droplet temperature, the chamber temperature, and the liquid metal emissivity[23].

Governing Equation Integration

The equations for droplet dynamics and thermodynamics described above result in a set of five ordinary differential equations, two for velocity, two for position, and one for temperature. This set of equations is integrated in time using a predictor-corrector scheme described in Reference 24. The integration is initiated at the time of primary breakup for each droplet, and is continued until the droplet undergoes secondary breakup, cools to the solidification temperature, or exits the computational domain. The dynamics and thermodynamics of droplets generated as a result of secondary breakup are computed in the same manner as those of droplets generated by the primary breakup.

Secondary Breakup Model

The correlations used for the secondary breakup computations were obtained from Reference 25. In this reference, Hsiang and Faeth report the results of a very detailed investigation of the breakup of single droplets. The experiments were conducted in a shock tube, and numerous different liquids were used in order to produce data for a wide range of droplet conditions. The results of this investigation are correlations for breakup regimes, droplet breakup time, droplet deformation, and droplet size distribution after breakup.

Deformation and Breakup Regime

Hsiang and Faeth identify six regimes which characterize a droplet exposed to a moving fluid. Three of these regimes, No Deformation, Nonoscillatory Deformation, and Oscillatory Deformation, do not result in droplet breakup. The remaining three, Bag Breakup, Multimode Breakup, and Shear Breakup, do result in droplet breakup. The applicable breakup regime for any particular droplet is a function of its Weber number and Ohnesorge number. These dimensionless numbers represent the ratios of drag and liquid viscous forces to surface tension forces, respectively, and can be written:

$$We_d = \rho_g d_d U_{rel}^2 / \sigma_L \tag{8}$$

and

$$Oh_d = \mu_L / (\rho_L d_d \sigma_L)^{1/2} \tag{9}$$

The droplet deformation and breakup regime map obtained from Reference 25 is illustrated in Figure 4. This map is used by the droplet code to determine which droplets breakup during the atomization process.

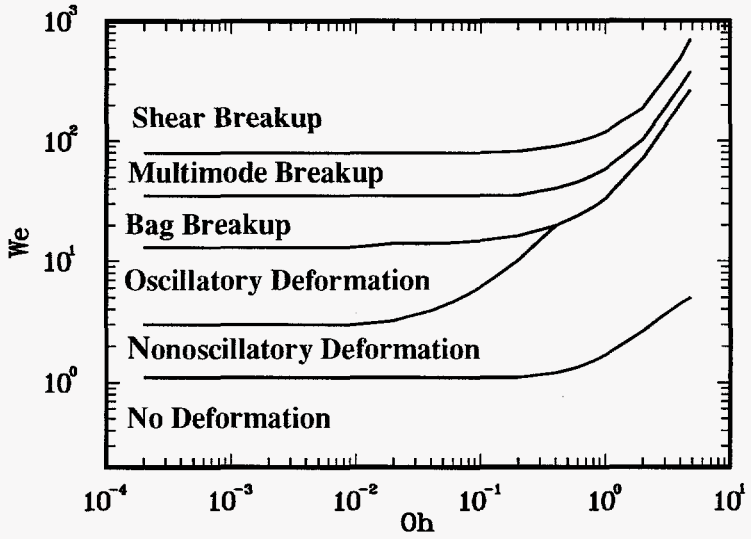

Figure 4: Breakup regime map.

Droplet Breakup Time

The time required for the droplet to undergo distortion and breakup has been correlated[25] as a function of Ohnesorge number and a characteristic breakup time:

$$t^* = d_d (\rho_L/\rho_g)^{1/2}/U_{rel} \tag{10}$$

The breakup time correlation is written in the form:

$$t_b/t^* = 5/(1 - Oh_d/7),\ We_d < 10^3 \tag{11}$$

This is used by the droplet code to determine how long to track a droplet through the flowfield prior to breakup.

Droplet Deformation

The distortion of the droplets prior to breakup has a significant effect on the droplet drag, and thus on the droplet breakup process. Hsiang and Faeth observed that the droplets flattened, with a resultant increase in cross-stream diameter, prior to breakup. The distortion of the droplets within the code is calculated from correlations derived by Hsiang and Faeth and based on their experimental data.

The initial step in calculating the droplet distortion is to determine the maximum droplet cross-stream diameter. For low Oh numbers (Oh < 0.1), Reference 25 presents:

$$d_{c,\,max}/d_0 = 1 + 0.19 We_d^{1/2} \tag{12}$$

In addition, Hsiang and Faeth present data for $d_{c,max}/d_0$ as a function of We_d in graphical form for $Oh_d = 1.5$ and 3.1. The distortion model within the code interpolates between these curves and the correlation shown above in order to determine the maximum cross-stream diameter. Figure 5 presents the correlation and the two curves used in this interpolation. The $d_{c,max}/d_0$ is limited to a value of 2 within the code, approximately the largest value reported by Hsiang and Faeth.

After the maximum possible distortion has been computed, a characteristic time, corrected for Ohnesorge number, is computed according to the relation:

$$t_C^* = t^*/(1 - Oh_d/7) \tag{13}$$

The ratio of current droplet distortion to maximum droplet distortion is then computed from a curve fit to data presented by Hsiang and Faeth of the form:

$$\frac{(d_c - d_0)}{(d_c - d_0)_{max}} = 0.615\left(t/t_c^*\right) \tag{14}$$

The droplet distortion is computed as the droplets are tracked through the flowfield. Based on Reference 25, the drag coefficient is varied between that of a sphere and that of a disk, depending upon the extent of droplet distortion.

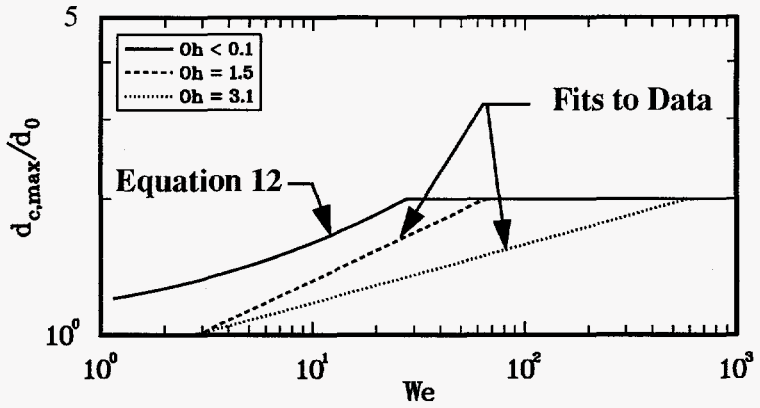

Figure 5: Droplet maximum distortion correlation.

Secondary Breakup Size Distribution

The size distribution of droplets following secondary breakup was also carefully measured by Hsiang and Faeth. Their results indicate that the droplets produced by bag breakup and multimode breakup fit the root-normal distribution of Simmons[15] with the ratio of mass median diameter to Sauter mean diameter equal to 1.2. The size distribution produced by shear breakup tends to follow the root-normal distribution for droplets smaller than the mass median diameter, but deviates significantly for droplets larger than the mass median diameter. The secondary breakup model within the atomization code assumes that the post-breakup droplets follow the root-normal distribution regardless of the breakup mode. This is done because computer simulations indicate that relatively few droplets undergo shear breakup, compared to bag and multimode breakup.

The assumption of the applicability of the root-normal distribution with the ratio of MMD to SMD equal to 1.2 results in the need to specify only the Sauter mean diameter for the complete droplet distribution to be specified. Hsiang and Faeth[25] developed a correlation for SMD from their extensive experimental data:

$$\rho_g SMD U_{rel}^2/\sigma_L = 6.2\,(\rho_L/\rho_g)^{1/4}\left[\mu_L/\left(\rho_L d_d U_{rel}\right)\right]^{1/2} We_d \tag{15}$$

The droplet code uses this correlation for SMD, in conjunction with the root-normal distribution, to perform the secondary breakup. Similar to the primary breakup technique, the mass of each computational droplet which undergoes secondary breakup is divided into bins, each of which represents droplets within a fixed size range. The amount of mass in each bin, and thus the number of droplets represented by each bin, is determined from the root-normal distribution. Subsequently, each bin is treated as a single computational droplet, representing multiple real droplets, for the remaining computations. Each of these computational droplets is released into the flowfield at the location of secondary breakup, with the same velocity and temperature as the parent droplet at the time of breakup.

Liquid Metal Properties

The various correlations used for the film, sheet, primary, and secondary breakup models rely extensively on the properties of the liquid being atomized. The properties of various liquid metals, as functions of temperature, were obtained from References 26 and 27. Properties of liquid alloys, as functions of temperature, are difficult to find in the literature. At present, weighted averages of the properties of the pure liquid metals which make up an alloy are used within the code to approximate that alloy's properties.

LIQUID METAL DROPLET SOLUTION

NIST Solution

The NIST atomization conditions presented in Table 1 and the INCA solution presented above were used as input conditions for the atomization code. With these conditions, all the inputs for the atomization code are specified, with the exception of the number of sheet segments to use during the sheet breakup process, the number of bins to use in the primary breakup process and the number of bins to use in the secondary breakup process. For the present simulation, each of these quantities was chosen to be 25. It was found through numerical experimentation that these values are large enough to give statistically significant results, yet are small enough to ensure that the solution remains manageable.

The film model within the code produced a film thickness of 0.102 mm and a film mean velocity of 2.05 m/sec at the edge of the metal delivery tube. The sheet model, using the film thickness and velocity as initial conditions, produced a value for the mean sheet length of 3.63 mm. The sheet trajectory is illustrated in Figure 6. Except for the portion of the sheet located very close to the delivery tube edge, the sheet follows the streamlines of the gas flowfield solution.

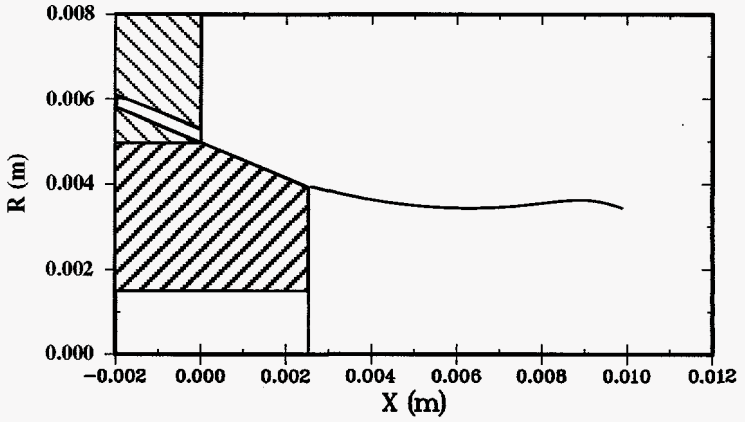

Figure 6: Sheet trajectory.

The 25 computational droplets released from each of the 25 sheet segments by primary breakup produced 625 computational droplets which were tracked through the gas flowfield solution shown in Figure 2. Figure 7 shows trajectories from selected computational droplets released during the primary breakup process. As observed experimentally by Anderson and Figliola[2], the droplets pass through the nozzle centerline as they proceed through the gas flowfield. Of the 625 computational droplets produced by the primary breakup process, 45 underwent secondary breakup into 25 additional computational droplets, resulting in a total of 1750 computational droplets for this case. All but one of these 45 secondary breakups occurred by bag breakup, and the remaining occurred by multimode breakup.

The droplets produced by the computational model were numerically sieved into bins with size limits identical to those used to sieve the powder produced experimentally at NIST, and characteristic particle diameters were computed. A comparison between these characteristic diameters and those obtained experimentally at NIST[4] is presented in Table 2.

Table 2: Comparison of NIST Experimental Results and Code Predictions

Quantity	Common Name	NIST Measurement	Code Prediction
D[1,0]*	Arithmetic Mean	9.39 μm	15.90 μm
D[2,0]	Surface Mean	10.98 μm	19.09 μm
D[2,1]	Length Mean	12.85 μm	22.93 μm
D[3,0]	Volume Mean	14.18 μm	22.18 μm
D[3,2]	Sauter Mean	23.65 μm	29.95 μm
D[4,3]	Herdan Mean	46.30 μm	36.36 μm
D[V,10]	10% Diameter	9.14 μm	19.10 μm
D[V,50]	Mass Median Diameter	37.77 μm	34.26 μm
D[V,90]	90% Diameter	95.73 μm	55.87 μm

* $D[a,b] = \left[\frac{\sum N_i D_i^a}{\sum N_i D_i^b}\right]^{1/(a-b)}$ where i is the size range, N_i is the number of particles in that size range, and D_i is the middle diameter of size range i. [28]

For this case, the predicted Sauter mean diameter is approximately 27 percent larger than the NIST data, and the predicted mass median diameter is approximately 9 percent smaller than the NIST data. These predictions are considered reasonably good considering the early stage of development of the atomization code.

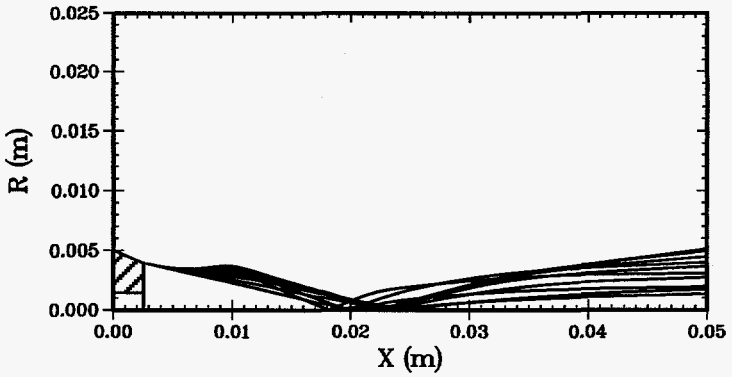

Figure 7: Selected droplet trajectories.

The particle size distribution produced by the computations is compared graphically to the NIST experimental data in Figure 8. In this figure, the particle size distribution predicted by the atomization code is significantly narrower than the experimental data, with relatively few submicron particles or particles larger than 125 microns predicted. The results of this narrow predicted size distribution can also be seen in the cumulative size distribution plot shown in Figure 9, in which the predicted distribution curve is significantly steeper than the experimental distribution curve. The exact cause of this discrepancy in the size distribution is not known at this time, but the trajectories shown in Figure 7 indicate that the large particles found in the experimental data could likely be caused by the collision and subsequent coalescence of droplets in the vicinity of the nozzle centerline. Secondary breakup of the resulting large droplets does not occur because the droplets have accelerated to a high velocity at this point in the flowfield, reducing the relative velocity between the droplets and the gas, and thus reducing the droplet Weber number to a value below the minimum breakup value shown in Figure 4.

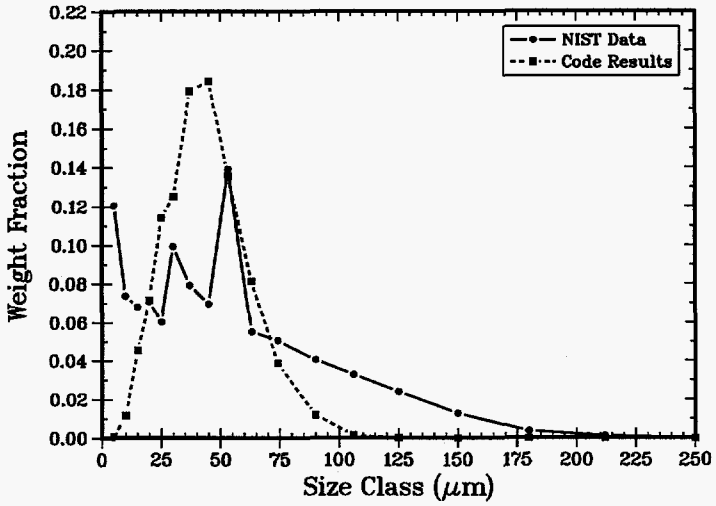

Figure 8: Comparison of NIST and code particle size distributions.

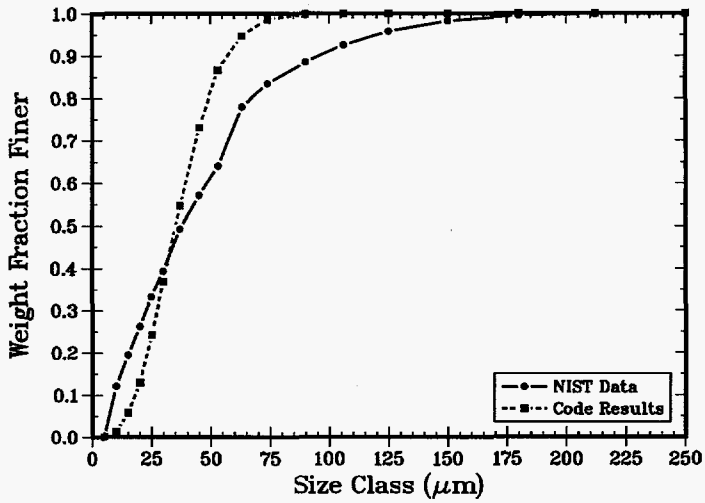

Figure 9: Comparison of NIST and code cumulative size distribution.

Parametric Study

A parametric study of the effects of varying liquid metal flow rate, liquid metal temperature, and nozzle stagnation pressure on particle size has been performed. The results of this study are presented in Figure 10 and are consistent with the experimental work presented in Reference 29. Mean and median particle sizes increase with increasing metal flow rate due to the resultant increase in film thickness, sheet thickness, and subsequent primary breakup diameters. Mean and median particle sizes decrease with increasing metal initial temperature due to the decrease in liquid viscosity and surface tension of the liquid and the effects of these properties on the film thickness and breakup diameters. Particle sizes decrease with increasing nozzle pressure (at a fixed metal flow rate) due to the higher gas velocities which result in thinner, higher velocity films and smaller mean breakup diameters.

SUMMARY

A technique for numerically simulating the flowfield and atomization process within a high pressure gas atomizer has been developed. The technique involves calculating the gas flowfield with a Navier-Stokes program, and then solving for the characteristics of the atomizing metal using a separate program developed by the authors. The atomization code models the liquid metal film which forms on the end of

the delivery tube, the sheet of liquid metal which forms as the film breaks away from the delivery tube, the primary breakup of the sheet into droplets, the dynamics and thermodynamics of the droplets, and any secondary breakup of droplets which may occur. A comparison of the powder metal calculated by the code with data indicates that the atomization code is calculating values of the mass median diameter and Sauter mean diameter within 9 and 27 percent of the experimental values, respectively. However, the size distribution of the powder calculated by the code is significantly narrower than that of the experimental data. Droplet collision and coalescence can explain the existence of large particles seen in experimental data, and currently is not modeled within the code. Parametric studies of the effects of metal flow rate, initial metal temperature, and nozzle pressure produce trends which are consistent with experimental data.

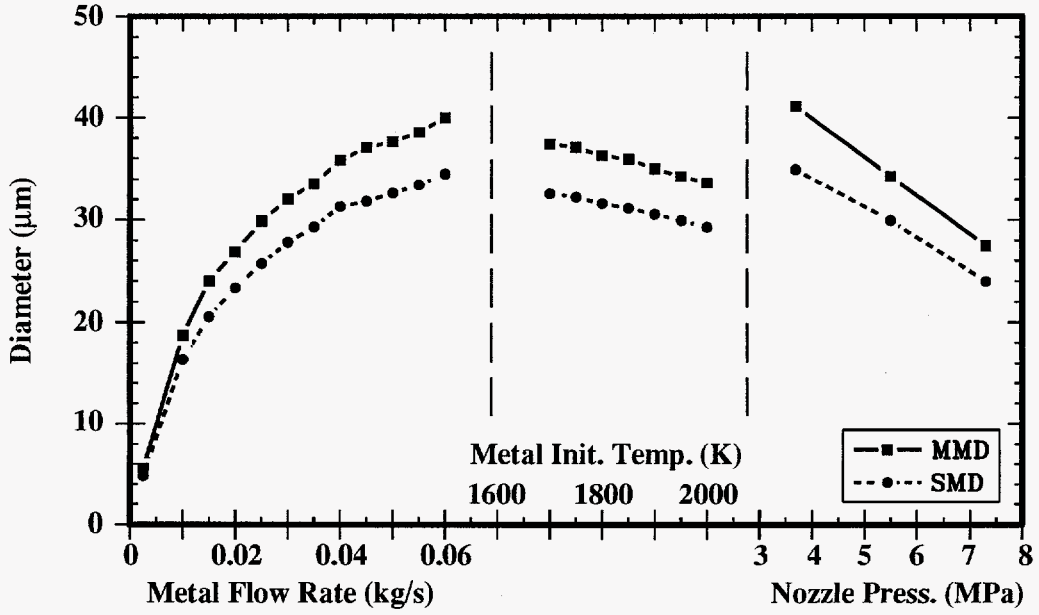

Figure 10: Effects of metal flow rate, metal initial temperature, and nozzle pressure on mass median diameter and Sauter mean diameter.

ACKNOWLEDGMENTS

This work was performed at Sandia National Laboratories which is operated for the Department of Energy under contract number DE-AC04-94AL85000. The authors wish to thank Dr. Stephen Ridder of NIST for the experimental data presented in this paper and his valuable input concerning the high pressure gas atomization process.

REFERENCES

[1] *INCA: 3D Multi-Zone Navier-Stokes Flow Analysis with Finite-Rate Chemistry, User's Manual Part 1: Input Guide,* Amtec Engineering, Inc., Bellevue, Washington, January 1992.

[2] I. E. Anderson and R. S. Figliola, "Observations of Gas Atomization Process Dynamics," *Modern Developments in Powder Metallurgy,* Vol. 20, Ed. P. U. Gummeson et al., 1988, pp. 205-223.

[3] C. B. Davies and E. Venkatapathy, "The Multidimensional Self-Adaptive Grid Code, SAGE," NASA Technical Memorandum 103905, 1992.

[4] S. D. Ridder, Department of Commerce, National Institute of Standards and Technology (NIST), Gaithersburg, Maryland, private communication, July 1994.

[5] B. Baldwin and T. Barth, "A One-Equation Turbulent Transport Model for High Reynolds Number Wall-Bounded Flows," NASA Technical Memorandum 102847, 1990.

[6] J. R. Viegas and M. W. Rubesin, "A Comparative Study of Several Compressibility Corrections to Turbulence Models Applied to High-Speed Shear Layers," AIAA 91-1783, June 1991.

[7] P. I. Espina, U. Piomelli, and G. E. Mattingly, "A Numerical Investigation of the Compressible Flow Field Produced in an Annular Jet, Close-Coupled, Gas Metal Atomizer," *Computational and Numerical Techniques in Powder Metallurgy*, Ed. D. S. Madan, I. E. Anderson, and W. E. Frazier, 1993, pp. 41-53.

[8] A. Ünal, "Flow Separation and Liquid Rundown in a Gas-Atomization Process," *Metallurgical Transactions B*, Vol. 20B, October 1989, pp. 613-622.

[9] A. Ünal, "Influence of Gas Flow on Performance of 'Confined' Atomization Nozzles," *Metallurgical Transactions B*, Vol. 20B, December 1989, pp. 833-843.

[10] A. Ünal, "Liquid Break-Up in Gas Atomization of Fine Aluminum Powders," *Metallurgical Transactions B*, Vol. 20B, February 1989, pp. 61-69.

[11] F. M. White, *Viscous Fluid Flow*, McGraw-Hill, Inc., New York, 1974.

[12] A. J. Chapman and W. F. Walker, *Introductory Gas Dynamics*, Holt, Rinehart, and Winston, Inc., New York, 1971.

[13] T. Arai and H. Hashimoto, in *Proceedings of the 3rd International Conference on Liquid Atomization and Spray Systems*, The Institute of Energy, London, 1985, pp. VIB/1/1-7.

[14] H. Eroglu, N. Chigier, and Z. Farago, "Coaxial Atomizer Liquid Intact Lengths," *Physics of Fluids A*, Vol. 3, No. 2, February 1991, pp. 303-308.

[15] H. C. Simmons, "The Correlation of Drop-Size Distributions in Fuel Nozzle Sprays," *Journal of Engineering for Power*, July 1977, pp. 309-319.

[16] P.-K. Wu, G. A. Ruff, and G. M. Faeth, "Primary Breakup in Liquid-Gas Mixing Layers," *Atomization and Sprays*, Vol. 1, 1991, pp. 421-440.

[17] K. E. Knoll and P. E. Sojka, "Flat-Sheet Twin-Fluid Atomization of High-Viscosity Fluids. Part I: Newtonian Liquids," *Atomization and Sprays*, Vol. 2, 1992, pp. 17-36.

[18] P. J. Thomas, "On the Influence of the Basset History Force on the Motion of a Particle Through a Fluid," *Physics of Fluids A*, Vol. 4, No. 9, September 1992, pp. 2090-2093.

[19] C. B. Henderson, "Drag Coefficients of Spheres in Continuum and Rarefied Flows," *AIAA Journal*, Vol. 14, No. 6, June 1976, pp. 707-708.

[20] A. B. Bailey and J. Hiatt, "Free-Flight Measurements of Sphere Drag at Subsonic, Transonic, Supersonic, and Hypersonic Speeds for Continuum, Transitional, and Near-Free-Molecular Flow Conditions," TR 70-291, Arnold Engineering Development Center, Arnold AF Station, Tennessee, March 1971.

[21] S. F. Hoerner, *Fluid-Dynamic Drag*, Hoerner Fluid Dynamics, Albuquerque, New Mexico, 1965.

[22] D. W. Kuntz and V. A. Amatucci, "Drag and Heating Modifications Implemented Within the PLUTO Computer Program," SAND92-2519, Sandia National Laboratories, Albuquerque, New Mexico, January 1993.

[23] F. Kreith, *Principles of Heat Transfer*, Intext Educational Publishers, New York, 1973.

[24] L. F. Shampine and H. A. Watts, "DEPAC - Design of a User Oriented Package of ODE Solvers," SAND79-2374, Sandia National Laboratories, Albuquerque, New Mexico, 1979.

[25] L.-P. Hsiang and G. M. Faeth, "Near-Limit Drop Deformation and Secondary Breakup," *International Journal of Multiphase Flow*, Vol. 18, No. 5, 1992, pp. 635-652.

[26] R. N. Lyon, *Liquid-Metals Handbook*, The Committee on the Basic Properties of Liquid Metals, Office of Naval Research, Department of the Navy, January 1954.

[27] T. Iida and R. I. L. Guthrie, *The Physical Properties of Liquid Metals*, Clarendon Press, Oxford, 1988.

[28] A. H. Lefebvre, *Atomization and Sprays*, Hemisphere Publishing Corporation, New York, 1989.

[29] A. Ünal, "Effect of Processing Variables on Particle Size in Gas Atomization of Rapidly Solidified Aluminum Powders," *Materials Science and Technology*, Vol. 3, December 1987, pp. 1029-1039.